Biosensors and Bioelectronics 241 (2023) 115665

Contents lists available at ScienceDirect

Biosensors and Bioelectronics

journal homepage: www.elsevier.com/locate/bios

Selective oxidation of p-phenylenediamine for blood glucose detection enabled by Se-vacancy-rich $TiSe_{2-x}$@Au nanozyme

Caixia Sun [a,b,e], Xue Zhang [b], Hao Huang [b,*], Ya Liu [a], Xianwei Mo [a], Yufei Feng [c], Jiahong Wang [b], Wenhua Zhou [b,d], Paul K. Chu [f], Xue-Feng Yu [b,d], Wenxin Liu [a,**]

[a] Zhanjiang Institute of Clinical Medicine, Zhanjiang Central Hospital, Guangdong Medical University, Zhanjiang, 524045, People's Republic of China
[b] Shenzhen Key Laboratory of Micro/Nano Biosensing, Shenzhen Institute of Advanced Technology, Chinese Academy of Sciences, Shenzhen, 518055, People's Republic of China
[c] Life Science and Technology School, Lingnan Normal University, Zhanjiang, 524048, People's Republic of China
[d] Biomedical Imaging Science and System Key Laboratory, Chinese Academy of Sciences, Shenzhen, 518055, People's Republic of China
[e] The First Clinical Medical School, Guangdong Medical University, Zhanjiang, 524023, People's Republic of China
[f] Department of Physics, Department of Materials Science and Engineering, and Department of Biomedical Engineering, City University of Hong Kong, Tat Chee Avenue, Kowloon, Hong Kong, People's Republic of China

ARTICLE INFO

Keywords:
Transition metal dichalcogenides
Se vacancies
Nanozymes
Selective oxidation
Glucose detection

ABSTRACT

Nanozymes with enzyme-like characteristics have drawn wide interest but the catalytic activity and substrate selectivity of nanozymes still need improvement. Herein, Se-vacancy-rich $TiSe_{2-x}$@Au nanocomposites are designed and demonstrated as nanozymes. The $TiSe_{2-x}$@Au nanocomposites show excellent peroxidase-like activity and the chromogenic substrate p-phenylenediamine (PPD) can be selectively oxidized to compounds that exhibit an absorption peak at 413 nm that differs from that of self-oxidation or generally oxidized species, suggesting high catalytic activity and strong substrate selectivity. Theoretical calculations reveal that the PPD adsorption geometry at Se vacancies with an adsorption energy of −3.00 eV shows a unique spatial configuration and charge distribution, thereby inhibiting the free reaction and promoting both the activity and selectivity in PPD oxidation. The $TiSe_{2-x}$@Au colorimetric system exhibits a wide linear range of 0.015 mM–0.6 mM and a low detection limit of 0.0037 mM in the detection of glucose. The blood glucose detection performance for human serum samples is comparable to that of a commercial glucose meter in the hospital (relative standard deviation $< 6\%$). Our findings demonstrate a new strategy for rapid and accurate detection of blood glucose and our results provide insights into the future design of nanozymes.

1. Introduction

Nanozymes are nanomaterials with enzyme-like characteristics (Wu et al., 2019). Compared with natural enzymes, artificial enzymes that combine the merits of natural enzymes and nanomaterials are considered the next generation of enzyme mimics because of simple production, low cost, good environmental stability, and specific catalytic activity (Jiao et al., 2020; Sengupta et al., 2020; Song et al., 2020). Since Yan et al. reported Fe_3O_4 with intrinsic peroxidase-like activity in 2007 (Gao et al., 2007), numerous nanomaterials have been demonstrated as nanozymes for different applications (Wu et al., 2019). For example, carbon quantum dots (Shamsipur et al., 2014), noble metals (Liu et al., 2021; Xue et al., 2021), metal-organic frameworks (Zhang et al., 2019), and two-dimensional (2D) materials (Song et al., 2010; Wu et al., 2020; Yu et al., 2018) with peroxidase, catalase, oxidase, and superoxide dismutase activities have attracted interest in simulating the efficient catalytic characteristics of natural enzymes pertaining to the degradation of organic chemicals, cancer treatments as well as biosensing. Although advances have been made, the catalytic activity and substrate selectivity of nanozymes still needs improvement (Wu et al., 2019). In addition, self-oxidation of the substrates in air generally distorts the signals (Liang and Han, 2020) and can cause errors in colorimetric systems which depend on the oxidization of chromogenic substrates such as 3,3′,5,5′-tetramethylbenzidine (TMB), 2,2′-azino-bis

* Corresponding author.
** Corresponding author.
E-mail addresses: hao.huang@siat.ac.cn (H. Huang), wenxin_liu@gdmu.edu.cn (W. Liu).

https://doi.org/10.1016/j.bios.2023.115665
Received 3 August 2023; Received in revised form 25 August 2023; Accepted 2 September 2023
Available online 9 September 2023

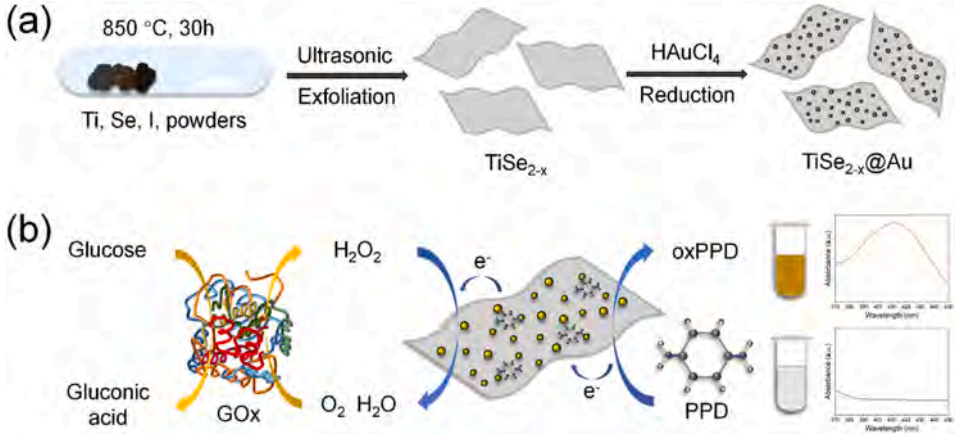

Scheme 1. (a) Synthesis of $TiSe_{2-x}$ and $TiSe_{2-x}$@Au nanocomposites and (b) Schematic diagram of glucose detection.

(3-ethylbenzthiazoline-6-sulphonic acid) (ABTS), o-phenylenediamine (OPD) and p-phenylenediamine (PPD), and so on (Li et al., 2020; Miao et al., 2019; Sengupta et al., 2020). Therefore, it is crucial to design and identify novel nanozymes with high catalytic activity and strong substrate selectivity.

Recently, transition metal dichalcogenides (TMDs) with the unique sandwich-like structure and tunable electronic properties have been produced in different forms (Khan et al., 2021; Rohaizad et al., 2021; Xu et al., 2021) and have large potential in electronic devices, catalysts, and sensors (Choi et al., 2017; Rohaizad et al., 2021; Zhang et al., 2021). Several types of TMDs and their hybrids have been reported to have the peroxidase-like activity. For example, Yu et al. have synthesized molybdenum disulfide (MoS_2) nanoflakes with different modifications, and TMB and ABTS are used as chromogenic substrates in the colorimetric analysis of H_2O_2 and glucose (Yu et al., 2018). Chen et al. have demonstrated that tungsten selenide (WSe_2) nanosheets possess peroxidase-like properties under acidic conditions and developed a sensitive and selective colorimetric method for glucose detection (Chen et al., 2017). By using Au nanoparticles (AuNPs), Hong et al. have designed a sensitive colorimetric analysis for the detection of glucose, and the peroxidase-like activity of the Au@WSe_2 nanostructure is enhanced significantly by the synergistic catalytic effects of AuNPs and WSe_2 nanosheets (Hong et al., 2021). Jiang et al. have proposed that dextran-decorated molybdenum selenide ($MoSe_2$) can promote the peroxidase-like catalytic activity of $MoSe_2$ nanosheets at neutral pH for high-performance colorimetric glucose detection (Jiang et al., 2020). Singh et al. have shown that Ce-substituted $MoSe_2$ possesses high peroxidase-like activity as well as great affinity to TMB and H_2O_2, and the Ce-$MoSe_2$ composites with persistent peroxidase-mimic are suitable for accurate colorimetric glucose detection in serum (Singh et al., 2022). Although these previous works suggest great potential for TMDs as nanozymes, the substrate selectivity for TMDs and self-oxidation of the substrates need improvement. Moreover, the cost of nanozymes should be considered. However, Mo and W metals are relatively expensive and thus cost-efficient TMD such as $TiSe_2$ could be a better choice.

Surface engineering such as the incorporation of internal or artificial active sites plays an important role in optimizing the physical and chemical properties of 2D materials (Hong et al., 2017; Jiao et al., 2020; Lu et al., 2016). Vacancies are typical local structural disorders of point defects with unique electronic states which localize electrons near the defect area and produce defect energy levels to form charge-capturing centers for catalysis in 2D materials (Chang et al., 2021; Ling et al., 2021; Yao et al., 2020). The larger active surface area and enhanced electron transport resulting from rich vacancies improve the catalytic properties of 2D materials and endow some 2D materials with excellent enzyme-like activities (Shen et al., 2022). In addition, the adsorption behavior of substrates can be mediated by vacancy sites of TMDs and the vacancies have been proven to facilitate chemo-selectivity (Han et al., 2018; Sun et al., 2019). The combination of vacancy-enhanced catalysis and chemo-selectivity may promote the catalytic activity and substrate selectivity of TMDs-based nanozymes.

Diabetes mellitus (DM) is a chronic disease of abnormal elevated blood glucose caused by impaired insulin secretion by pancreatic β cells or peripheral insulin resistance (Kim et al., 2021; Pullano et al., 2022) and known to increase the risk of cancer, solid tumors, as well as hematological malignancies (Gong et al., 2021; Hussein et al., 2019; Kyriakou et al., 2021; Via et al., 2020). Therefore, it is necessary to perform long-term, continuous, and real-time blood glucose monitoring. Herein, Se-vacancy-rich $TiSe_{2-x}$@Au nanocomposites with high catalytic activity and strong substrate selectivity for glucose colorimetric detection are designed and demonstrated as nanozymes (Scheme 1). The peroxidase-like activity of the $TiSe_{2-x}$@Au nanocomposites is investigated and the chromogenic substrate PPD is selectively oxidized to special compounds like quinone compounds which differ from self-oxidized or generally oxidized species. Experimental and computational studies indicate the important roles of Se vacancies in the substrate selective reaction. By coupling with glucose oxidase (GOx), the $TiSe_{2-x}$@Au colorimetric system produces satisfactory results in glucose detection such as a wide linear range and low detection limit. To evaluate the practical feasibility, the $TiSe_{2-x}$@Au nanocomposites are used on real human serum samples. The results reveal a new technique for the rapid and accurate detection of blood glucose and provide insights into the design of nanozymes with high catalytic activity and substrate selectivity.

2. Materials and methods

2.1. Materials

Chemical and biological reagents. Glycine (Gly), p-phenylenediamine (PPD), glutathione (GSH), potassium chloride (KCl), sodium chloride (NaCl), zinc chloride ($ZnCl_2$) and anhydrous magnesium sulfate ($MgSO_4$), titanium powders, selenium particles, iodine, and chloroauric acid ($HAuCl_4 \bullet 3H_2O$) were purchased from Aladdin (Shanghai, China). Anhydrous calcium chloride ($CaCl_2$) was provided by Macklin (Shanghai, China) and D (+)-Glucose, urea, citric acid (CA), glucose oxidase (GOx), and sodium borohydride ($NaBH_4$) were obtained from Sigma Aldrich. Hydrogen peroxide (H_2O_2, 30%), sucrose (Suc), N, N-dimethylformamide (DMF), and absolute ethanol were provided by Shanghai Lingfeng Chemical Reagent Co., Ltd. L-Ascorbic acid (AA), sodium hydroxide (NaOH), and barium hydroxide ($Ba(OH)_2$) were purchased from Shanghai Hushi Chemical Co., Ltd. Sulfuric acid (H_2SO_4, 98%) and the acetic acid/sodium acetate buffer (HAc-NaAc) were bought from Dongjiang Reagent. All the chemicals were used as received

and distilled water was used to prepare the solutions.

Serum samples. The serum samples were collected from Zhanjiang Central Hospital, Guangdong Medical University (Zhanjiang, China). All the experiments were performed in accordance with the Guidelines of Clinical Sample Management Rules of Zhanjiang Central Hospital, Guangdong Medical University and approved by the Ethics Committee at Zhanjiang Central Hospital, Guangdong Medical University (IIT-2023-021-01). Before analysis, the samples were treated with $Ba(OH)_2$ and H_2SO_4 and diluted with distilled water (pH = 5.6).

2.2. Synthesis of $TiSe_{2-x}$ nanosheets and $TiSe_{2-x}$@Au nanocomposites

Synthesis of $TiSe_{2-x}$ nanosheets. The $TiSe_{2-x}$ nanosheets were synthesized by a simple ultrasonic method using $TiSe_2$ powders as the raw materials which were prepared by a modified chemical vapor transport method (Li et al., 2016). The titanium powders (0.9 g) and selenium particles (2.97 g) were sealed in a vacuum quartz tube with iodine (30 mg) as a transport agent and the tube was heated at 850 °C for 1800 min. Subsequently, it cooled naturally to room temperature to obtain high-quality $TiSe_2$ powders. After grinding in the DMF solution, the $TiSe_2$ solution (1 mg/mL) was sonicated for 10 h at 600 W for 2 s with an interval of 4 s. The mixture was continuously sonicated in an ultrasonic bath for 5 h (300 W). Finally, the $TiSe_{2-x}$ solution was centrifuged at 5000 rpm for 10 min and the supernatant was centrifuged at 10,000 rpm for 10 min to acquire the $TiSe_{2-x}$ nanosheets which were re-dispersed in absolute ethanol for further use.

Synthesis of $TiSe_{2-x}$@Au nanocomposites. The $TiSe_{2-x}$@Au nanocomposites were synthesized by a simple reduction process using the $TiSe_{2-x}$ nanosheets. 100 μL of the $TiSe_{2-x}$ nanosheets (2.73 mg/mL) were added to 5 mL of the $HAuCl_4$ (0.2 mM) solution at room temperature, followed by the addition of 150 μL of $NaBH_4$ (10 mM) and stirring for 3 min. The mixture was centrifuged at 8000 rpm for 5 min and the precipitate was washed with distilled water, DMF, and absolute ethanol successively 2–3 times to remove excess $HAuCl_4$. $TiSe_{2-x}$@Au nanocomposites were obtained and re-dispersed in 100 μL of absolute ethanol (4.09 mg/mL). The Au NPs were synthesized without the addition of $TiSe_{2-x}$ nanosheets.

2.3. Peroxidase-like activity measurement

The peroxidase-like activity of the $TiSe_{2-x}$ nanosheets and $TiSe_{2-x}$@Au nanocomposites was determined in the presence of the chromogenic substrate PPD and H_2O_2. 200 μL of PPD (20 mM) and 20 μL of H_2O_2 (50 mM) were added to a centrifuge tube, followed by the addition of 20 μL of $TiSe_{2-x}$ nanosheets (2.73 mg/mL) or $TiSe_{2-x}$@Au nanocomposites (4.09 mg/mL). Distilled water (260 μL) was added to reach a volume of 500 μL. The supernatant after the reaction was diluted 2 times and placed on a 96-well plate. The absorption spectra were recorded by the full wavelength microplate reader.

2.4. Colorimetric H_2O_2 detection

200 μL of PPD (50 mM), 20 μL of different concentrations of H_2O_2 (0.1 mM, 0.5 mM, 1 mM, 3 mM, 5 mM, 8 mM, 10 mM, 12 mM, 12.5 mM, 20 mM, 25 mM, 50 mM and 125 mM), 20 μL of $TiSe_{2-x}$@Au nanocomposites, and 260 μL of distilled water were added to the centrifuge tube sequentially, the final concentrations of H_2O_2 are 0.004 mM, 0.02 mM, 0.04 mM, 0.12 mM, 0.2 mM, 0.32 mM, 0.4 mM, 0.48 mM, 0.5 mM, 0.8 mM, 1 mM, 2 mM and 5 mM. After reacting at 40 °C for 40 min, the mixture was centrifuged at 10,000 rpm for 5 min and the supernatant was diluted 2 times and placed on a 96-well plate (200 μL). The absorbance intensity at 413 nm was measured.

2.5. Colorimetric glucose detection

15 μL of different concentrations of glucose (0.5 mM, 1 mM, 2 mM, 4 mM, 6 mM, 10 mM, 15 mM, 20 mM, 25 mM, 30 mM and 33.3 mM), 22.5 μL of GOx (1 mg/mL) and 12.5 μL of distilled water were mixed and incubated in a dark environment at 40 °C for 30 min. 200 μL of PPD (50 mM), 20 μL $TiSe_{2-x}$@Au nanocomposites, and 230 μL of distilled water were added successively, the final concentrations of glucose are 0.015 mM, 0.03 mM, 0.06 mM, 0.12 mM, 0.18 mM, 0.3 mM, 0.45 mM, 0.6 mM, 0.75 mM, 0.9 mM and 1 mM. The reaction proceeded at 40 °C for 40 min and the subsequent steps were the same as those in the previous H_2O_2 detection. The absorbance at 413 nm was measured. Another selectivity test for glucose was carried out by comparing with common interferences such as biomolecules and metal ions.

2.6. Glucose detection in serum samples

The human serum samples were treated with 0.1 M $Ba(OH)_2$ and 0.1 M H_2SO_4 (volume ratio 1:1) for 10 min and diluted 30 times with distilled water. The diluted serum samples were centrifuged at 10,000 rpm for 20 min to separate the supernatant. Subsequently, 180 μL of GOx (1 mg/mL) and 60 μL of distilled water were added to the supernatant and incubated in a dark environment at 40 °C for 30 min. 200 μL of PPD (50 mM), 20 μL of $TiSe_{2-x}$@Au nanocomposites and 80 μL of distilled water were added to 200 μL of the solution and reacted for 40 min at 40 °C. The subsequent steps were the same as those in glucose detection and the absorbance at 413 nm was measured.

2.7. Calculation

The density-functional theory (DFT) calculation was performed using the Vienna ab initio simulation program (VASP) and the projected augmented wave (PAW) (BlÖchl, 1994) pseudopotentials and Perdew-Burke-Ernzerhof (PBE) functional were used (Perdew, et al., 1996). The (001) surface of $TiSe_2$ was cleaved with three atomic layers and modeled with a p(4 × 4) periodic slab. A vacuum layer of 20 Å between neighboring slabs was used to avoid self-interactions. The energy cutoff was set as 450 eV for the plane-wave basis set. Brillouin zone sampling was restricted to the Monkhorst-Pack k-points sampling of 3 × 3 × 1 and the convergence threshold for electronic steps in geometry optimization was 1×10^{-5} eV. When the forces on each atom were below 0.02 eV/Å, the geometries were thought to converge. A frequency analysis was performed in the stable states in order to confirm that these represent genuine minima. All of the electronic energies were corrected for the zero-point energy (ZPE) contributions.

2.8. Characterization

Transmission electron microscopy (TEM), high-resolution TEM (HR-TEM), high-angle annular dark-field (HAADF) images, and elemental mappings were performed on the FEI Talos F200X at 200 kV (FEI, USA). Scanning electron microscopy (SEM) was conducted on the ZEISS SUPRA 55 (Carl Zeiss, Germany) and the atomic force microscopy (AFM) images were acquired on the Cypher S AFM (Asylum Research, USA). The powder X-ray diffraction (XRD) patterns were collected on a SmartLab X-ray diffractometer with Cu Kα radiation (40 kV, 30 mA) (Rigaku, Japan). The absorption spectra were acquired by UV-vis spectrophotometry on the TU-1810 (Purkinje General Instrument Co. Ltd. Beijing, China) and full wavelength microplate reader (Multiskan Sky with Curette and Touch Screen, Thermo Fisher Scientific, USA). The mass spectra were acquired by time-of-flight mass spectrometry (TOF, Thermo Fisher, USA), and X-ray photoelectron spectroscopy (XPS) was conducted on the Thermo Fisher ESCALAB 250Xi (Thermo Fisher, USA). The electron paramagnetic resonance (EPR) measurement was performed on a Bruker ESP-300 spectrometer (Bruker, Germany).

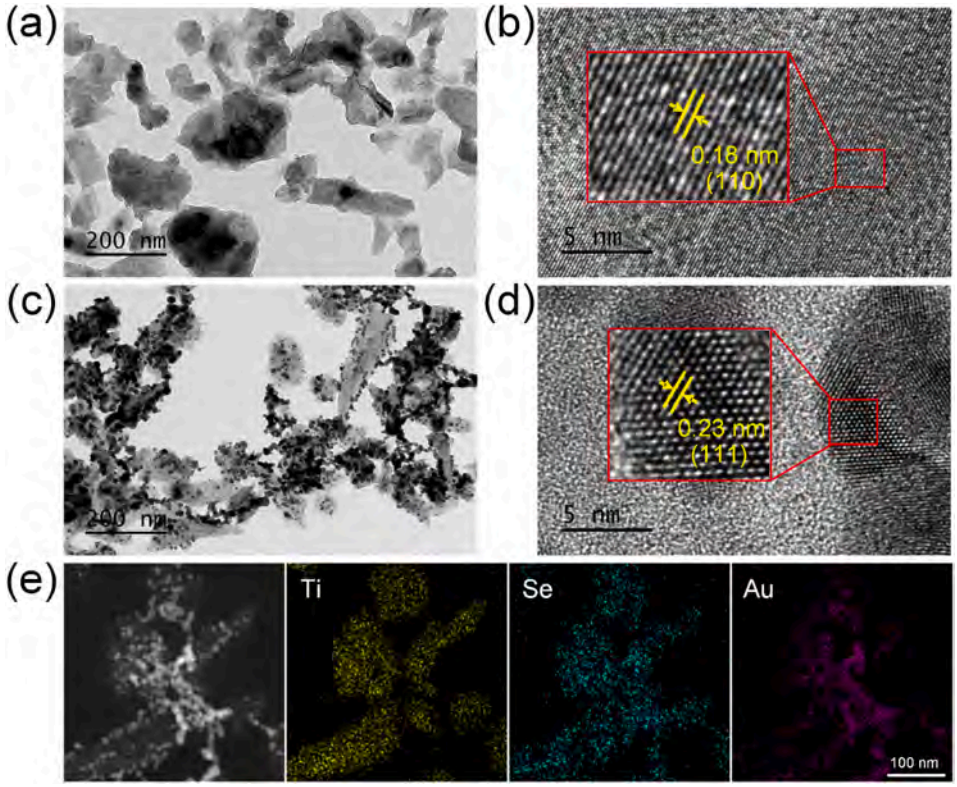

Fig. 1. (a, b) TEM and HR-TEM images of the $TiSe_{2-x}$ nanosheets, (c, d) TEM and HR-TEM images of the $TiSe_{2-x}$@Au nanocomposites, and (e) HAADF image and elemental maps of $TiSe_{2-x}$@Au nanocomposites.

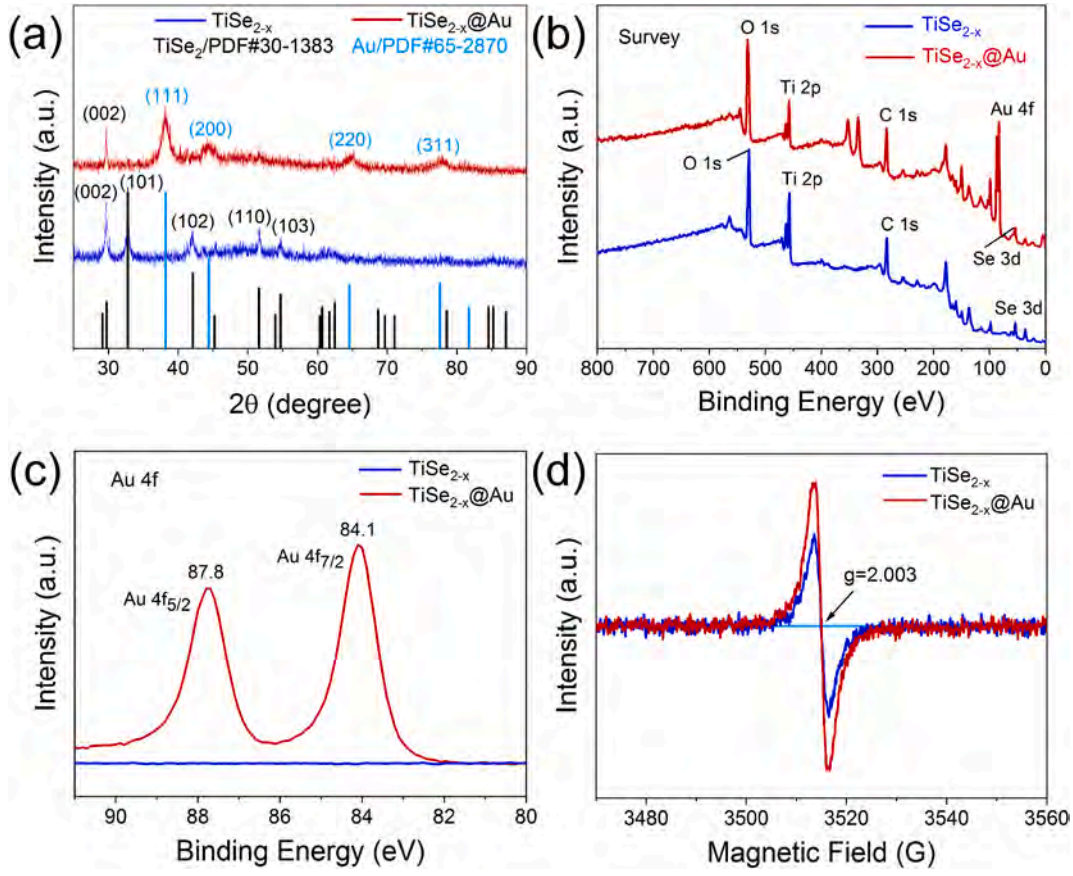

Fig. 2. (a) XRD patterns, (b) XPS survey spectra, (c) Au 4*f* spectra, (d) EPR spectra of the $TiSe_{2-x}$ nanosheets and $TiSe_{2-x}$@Au nanocomposites.

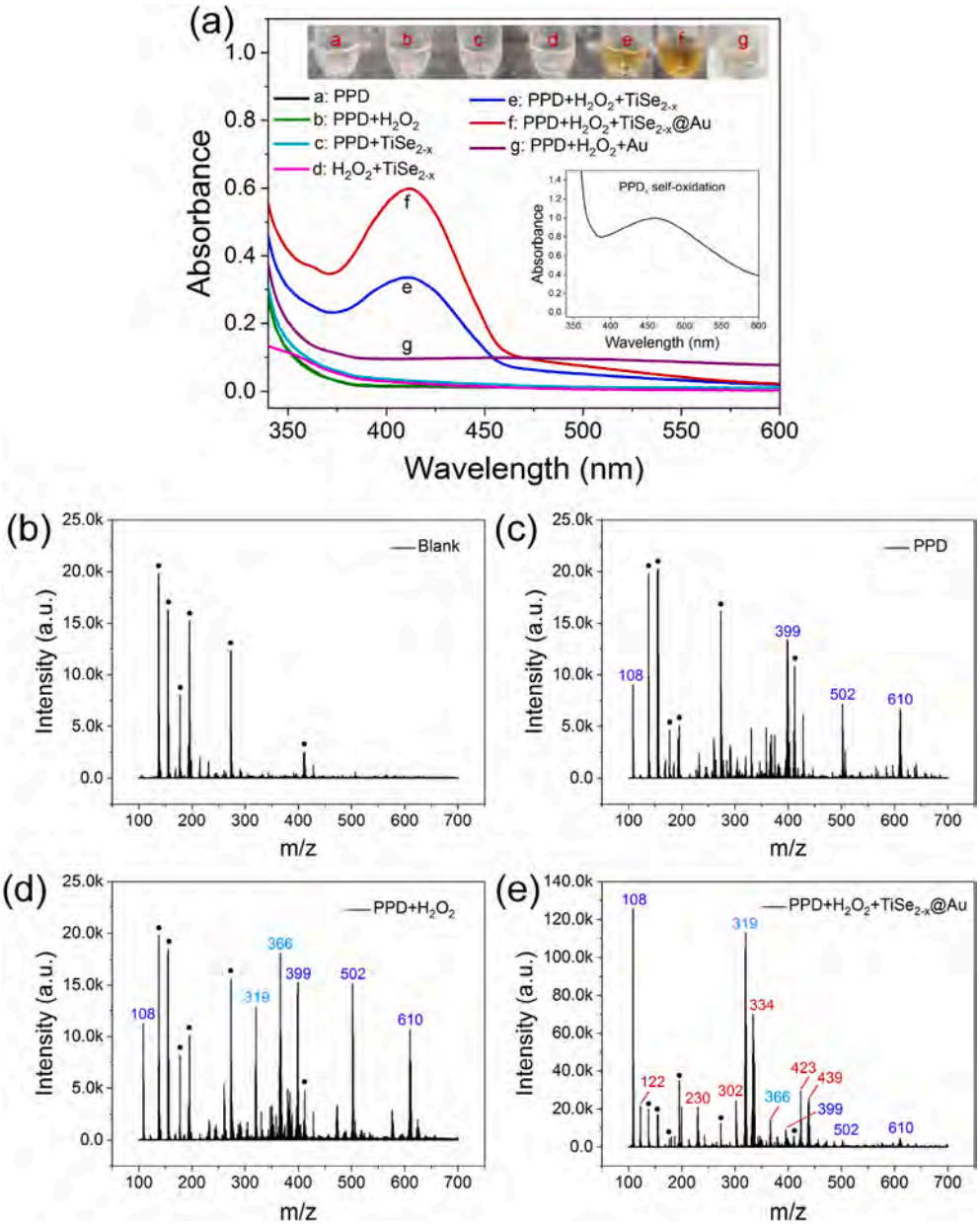

Fig. 3. (a) UV-vis spectra and photos of PPD, PPD + H_2O_2, PPD + $TiSe_{2-x}$, H_2O_2 + $TiSe_{2-x}$, PPD + H_2O_2 + $TiSe_{2-x}$, PPD + H_2O_2 + $TiSe_{2-x}$@Au and PPD + H_2O_2 + Au (Inset: self-oxidation of PPD); TOF spectra of (b) blank control, (c) PPD solution, (d) PPD + H_2O_2 system product, (e) PPD + H_2O_2 + $TiSe_{2-x}$@Au system product.

3. Results and discussion

3.1. Characterization of $TiSe_{2-x}$ nanosheets and $TiSe_{2-x}$@Au nanocomposites

The as-prepared $TiSe_2$ powders show a brown color and the typical layered structure according to SEM (Fig. S1a). The high crystal quality is confirmed by XRD. As shown in Fig. S1b, the XRD pattern of the $TiSe_2$ powders exhibits peaks at 29.71°, 32.78°, 42.08°, 45.24°, 51.60°, 54.70°, and 61.70° corresponding to the (002), (101), (102), (003), (110), (103) and (004) planes, respectively (PDF#30–1383). Benefiting from the layered structure of $TiSe_2$, the $TiSe_{2-x}$ nanosheets can be easily prepared by ultrasonic exfoliation. As shown by the AFM image (Fig. S2), the exfoliated $TiSe_{2-x}$ nanosheets have a thickness between 10 nm and 45 nm. After the growth of AuNPs on $TiSe_{2-x}$ nanosheets, the color of the $TiSe_{2-x}$ nanosheets dispersion changes from grey-green to light purple (Fig. S3a), and a new absorption peak at 550 nm from AuNPs emerge (Fig. S3b), indicating that the $TiSe_{2-x}$@Au nanocomposites have been fabricated.

The morphology of the $TiSe_{2-x}$ nanosheets and $TiSe_{2-x}$@Au nanocomposites is examined by TEM. The $TiSe_{2-x}$ nanosheets have a sheet-like structure (Fig. 1a) with a lattice spacing of 0.18 nm corresponding to the (110) plane of $TiSe_2$ (Fig. 1b) (Zhang et al., 2018). Compared with the $TiSe_{2-x}$ nanosheets, the $TiSe_{2-x}$@Au nanocomposites are decorated with dense AuNPs on the surface of the $TiSe_{2-x}$ nanosheets (Fig. 1c) and the lattice spacing of 0.23 nm stems from the (111) plane of Au (Fig. 1d) (Liu et al., 2020). The high-angle annular dark-field (HAADF) image and elemental maps are presented in Fig. 1e. The strong HAADF image contrast agrees with the different elements of Au and $TiSe_{2-x}$ and the distributions of Ti, Se, and Au confirm the successful fabrication of the $TiSe_{2-x}$@Au nanocomposites.

The crystal structure of the $TiSe_{2-x}$ nanosheets and $TiSe_{2-x}$@Au nanocomposites is studied by XRD. As shown in Fig. 2a, the broad peaks of the (002), (101), (102), (110) and (103) crystalline planes belong to

$TiSe_2$ in the $TiSe_{2-x}$ nanosheets, suggesting retainment of the parent structure. Moreover, the (111), (200), (220), and (311) crystalline planes of AuNPs (PDF#65–2870) as well as the (002) plane of $TiSe_2$ of the $TiSe_{2-x}$@Au nanocomposites can be observed. XPS is used to determine the compositions of the $TiSe_{2-x}$ nanosheets and $TiSe_{2-x}$@Au nanocomposites (Fig. 2b, c and Fig. S4). Ti and Se are detected from the $TiSe_{2-x}$ nanosheets and Ti, Se, and Au from the $TiSe_{2-x}$@Au nanocomposites (Fig. 2b). Fig. 2c shows two peaks at 84.1 eV and 87.8 eV from the $TiSe_{2-x}$@Au nanocomposites for Au 4 $f_{7/2}$ and Au 4 $f_{5/2}$, respectively, but no Au peaks can be found from the $TiSe_{2-x}$ nanosheets. The ratios of Ti to Se in both the $TiSe_{2-x}$ nanosheets and $TiSe_{2-x}$@Au nanocomposites are close to 1, which is larger than that of $TiSe_2$, indicating the introduction of Se vacancies. The abundant vacancies may be created by the long-time sonication process (Cai et al., 2018). The Ti 2*p* and Se 3*d* spectra of the $TiSe_{2-x}$@Au nanocomposites shift to lower binding energies compared to the $TiSe_{2-x}$ nanosheets (Fig. S4), suggesting more Se vacancies (Shen et al., 2022). This is confirmed by the EPR spectra. The $TiSe_{2-x}$@Au nanocomposites show a stronger EPR signal with a *g* value of 2.003 than the $TiSe_{2-x}$ nanosheets (Fig. 2d), indicating that hybridization of AuNPs facilitates the generation of Se vacancies. All these results suggest the successful synthesis of the Se-vacancy-rich $TiSe_{2-x}$ nanosheets and $TiSe_{2-x}$@Au nanocomposites.

3.2. Peroxidase-like activity of $TiSe_{2-x}$ nanosheets and $TiSe_{2-x}$@Au nanocomposites

The peroxidase-like activity of the $TiSe_{2-x}$ nanosheets and $TiSe_{2-x}$@Au nanocomposites are investigated using PPD. It has been reported that oxPPD (oxidized form of PPD) exists in the forms of free base and protonated species with absorption peaks at 460 nm and 530 nm–540 nm, respectively, and the broad absorbance at 500 nm–510 nm is believed to be due to the two forms of oxPPD (Cheng et al., 2019; Sun et al., 2018; Zhang et al., 2017). However, the self-oxidation of PPD under ambient conditions also contributes to the absorption peak at 460 nm (inset in Fig. 3a) and may bring uncertainties to the final colorimetric results. In this work, a special oxPPD absorption peak at 413 nm is observed (Fig. 3a). Under the same conditions, compared with PPD, PPD + H_2O_2, PPD + $TiSe_{2-x}$, and H_2O_2 + $TiSe_{2-x}$, the PPD + H_2O_2 + $TiSe_{2-x}$, PPD + H_2O_2 + $TiSe_{2-x}$@Au and PPD + H_2O_2 + Au show significant changes from colorless to brown-yellow and light-yellow (Fig. 3a), respectively. It should be noted that the PPD + H_2O_2 + Au only exhibits a broad absorption peak at around 460 nm, suggesting that the AuNPs have no selectivity in the oxidation of PPD compared with self-oxidation of PPD. Moreover, the absorption intensity at 413 nm of PPD + H_2O_2 + $TiSe_{2-x}$@Au is about twice that of PPD + H_2O_2 + $TiSe_{2-x}$, indicating a higher catalytic ability for the $TiSe_{2-x}$@Au nanocomposites. The high catalytic ability of $TiSe_{2-x}$@Au nanocomposites is probably due to the enhanced electron transport resulting from rich vacancies and decorated AuNPs as well as the quantum effect of the nanocomposites (Hong et al., 2021; Shen et al., 2022). This selective reaction can avoid the interference from possible self-oxidation of PPD and the $TiSe_{2-x}$@Au nanocomposites can serve as nanozymes.

To explore the mechanism of the specific reaction, the products of the PPD solution, PPD+H_2O_2, and PPD+H_2O_2+$TiSe_{2-x}$@Au are analyzed by TOF. Compared with the blank control group (Fig. 3b), multiple peaks at m/z 108, 399, 502, and 610 are observed from the PPD solution (Fig. 3c), and the intensity increases. New peaks at m/z 319 and 366 are observed in the presence of H_2O_2 indicative of oxidation and polymerization of PPD molecules (Fig. 3d). As for the $TiSe_{2-x}$@Au nanocomposites, new peaks at m/z 122, 230, 302, 334, 423, and 439 are observed from the colorimetric solution, and the intensity of the peaks at m/z 108 and 319 are higher than those of the PPD + H_2O_2 system (about 10 times enhancement) (Fig. 3e). Moreover, the intensity of the peaks at m/z 399, 502, and 610 decreases by about four times, suggesting the high catalytic ability and selectivity of the $TiSe_{2-x}$@Au nanocomposites. These results indicate that a special reaction pathway in the presence of

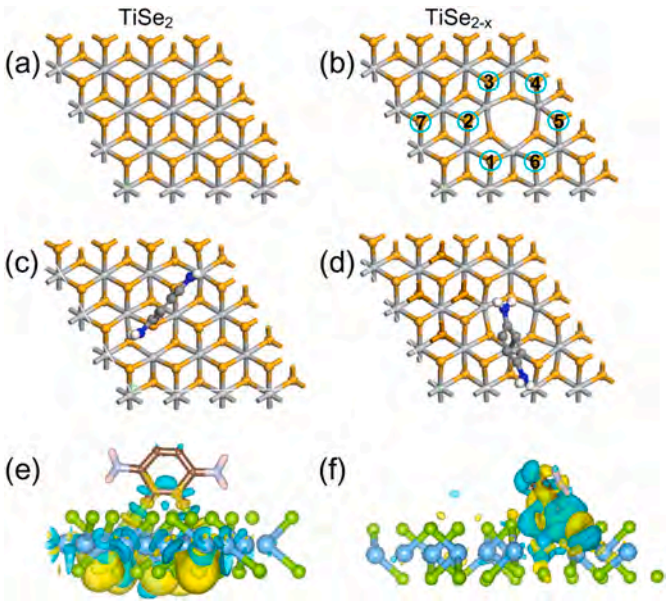

Fig. 4. (a, b) Simulated structures of $TiSe_2$ and possible adsorption Se sites (1–7) in $TiSe_{2-x}$, (c, d) Optimized geometries of PPD adsorbed on $TiSe_2$ and $TiSe_{2-x}$, and (e, f) Corresponding differential charge density of PPD adsorption on $TiSe_2$ and $TiSe_{2-x}$. The yellow and cyan regions represent electron accumulation and electron depletion, respectively.

$TiSe_{2-x}$@Au nanocomposites and the common pathway is inhibited. Generally, the oxidized products of PPD are mainly red-purple Bandrowski's base (BB) and yellow quinone compounds (Ritter and Schmitz, 1929). BB is susceptible to the pH and can be further oxidized to oxides. In the acidic environment, the concentration of quinone compounds is larger than that of BB (Ritter and Schmitz, 1929). In addition, the oxidized products of PPD may polymerize in various forms as the spatial configurations of oxide substrates changes, resulting in multiple new ion peaks (Durgaryan et al., 2013; Li et al., 2007; Urban et al., 2006). Therefore, it is believed that the absorption peak at 413 nm may arise from selectively oxidized yellow quinone compounds and various forms of oxPPD polymers.

DFT calculations are performed to understand the selectivity origin of Se vacancies in PPD oxidation. The (001) surface on $TiSe_2$ is shown in Fig. 4a and the Se-vacancy structure of $TiSe_{2-x}$ is simulated by removing a Se atom (Fig. 4b). The adsorption of PPD on $TiSe_2$ and $TiSe_{2-x}$ is then investigated and two adsorption geometries (Parallel and Vertical) are calculated on $TiSe_2$. Seven adsorption geometries caused by Se vacancies including three parallel adsorption sites (Parallel 1–2, Parallel 2–7 and Parallel 6–34) and four vertical adsorption sites (Vertical 1–2, Vertical 6-2, Vertical 6-3 and Vertical 2–7) are optimized. The adsorption energies of PPD on these sites are shown in Table S1 and Table S2. The PPD prefers to adsorb vertically on $TiSe_2$ with an adsorption energy of −2.82 eV as shown in Fig. 4c. Compared with $TiSe_2$, Fig. 4d shows the vertical 6-3 adsorption geometry at an oblique angle with an adsorption energy of −3.00 eV for $TiSe_{2-x}$ after structural optimization. The smaller adsorption energy of PPD on $TiSe_{2-x}$ suggests that the PPD molecule prefers to adsorb in the presence of Se vacancies. It should be noted that one end of the tilted PPD molecule almost inserts into the Se vacancy and only the remaining end can contact the free PPD molecules. This unique spatial configuration (6-3) of PPD on $TiSe_{2-x}$ undoubtedly increases the steric hindrance for the contacting among free PPD molecules and inhibits the free reaction between PPD molecules. This may be responsible for the selective reaction by $TiSe_{2-x}$. Differential charge density of PPD adsorption on $TiSe_2$ and $TiSe_{2-x}$ further confirms the charge distributions (Fig. 4e and f). As shown, the charges accumulate around the PPD molecule on $TiSe_{2-x}$ more than on $TiSe_2$, indicating that the charges can transfer more easily from the Se vacancy to PPD, which is agreement

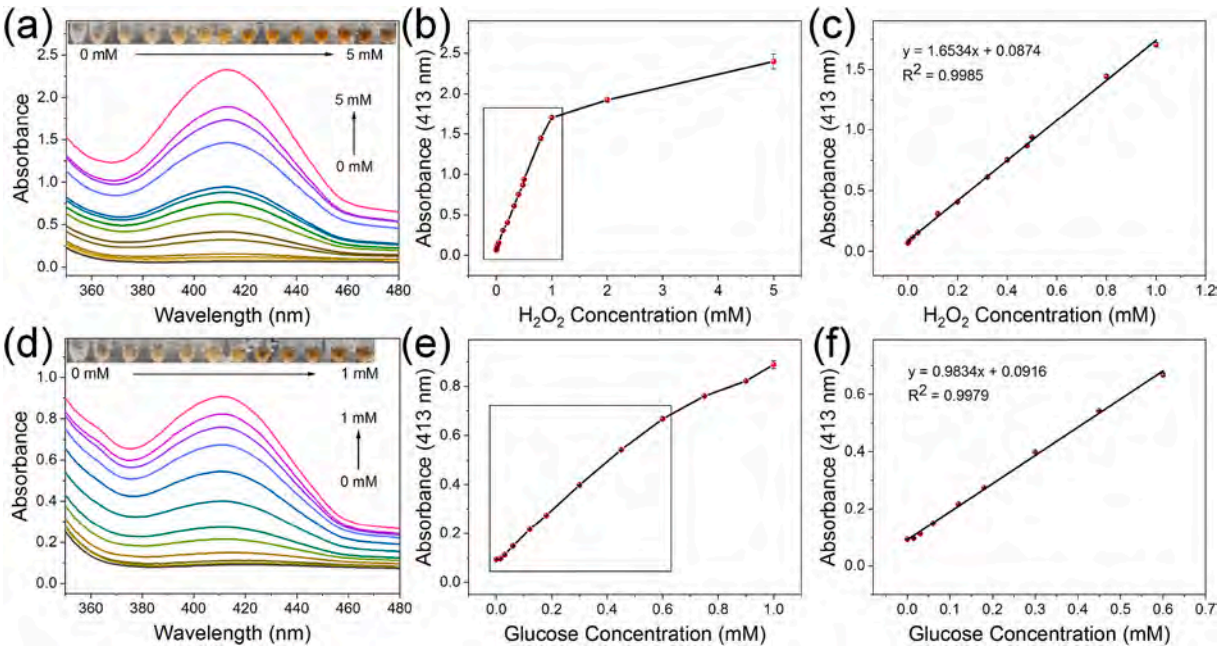

Fig. 5. (a) UV–vis spectra and corresponding photos of different concentrations of H_2O_2 (concentrations from bottom to top: 0.004, 0.02, 0.04, 0.12, 0.2, 0.32, 0.4, 0.48, 0.5, 0.8, 1, 2, 5 mM) for the $TiSe_{2-x}$@Au colorimetric system; (b) Changes in the peak intensity at 413 nm with increasing concentration of H_2O_2 (n = 3); (c) Linear plot of the absorbance at 413 nm versus concentration of H_2O_2 (n = 3); (d) UV-vis spectra and corresponding photos of different concentrations of glucose (concentrations from bottom to top: 0.015, 0.03, 0.06, 0.12, 0.18, 0.3, 0.45, 0.6, 0.75, 0.9, 1 mM) in the $TiSe_{2-x}$@Au colorimetric system; (e) Changes in the peak intensity at 413 nm with increasing concentration of glucose (n = 3); (f) Linear plot of the absorbance at 413 nm versus glucose concentration (n = 3).

with the stronger adsorption on $TiSe_{2-x}$. On the other hand, the more easily transferred charges in Se-vacancy rich $TiSe_{2-x}$ promote the selective reaction better compared to the back site of $TiSe_2$ (Chang et al., 2021).

Therefore, it is believed that the absorbance at 413 nm is caused by the selective catalysis of PPD by $TiSe_{2-x}$ or $TiSe_{2-x}$@Au. In other words, $TiSe_{2-x}$ has the peroxidase-like activity, and $TiSe_{2-x}$@Au further enhances the catalytic effect due to rapid charge transfer of AuNPs and synergistic quantum effects and hybrid structures (Liu et al., 2012, 2020). The enhanced selective catalysis of the $TiSe_{2-x}$@Au nanocomposites improves the sensitivity of the colorimetric method.

3.3. Colorimetric H_2O_2 detection and glucose detection

Experiments for the concentration of $TiSe_{2-x}$@Au nanocomposites, concentration of PPD, pH, reaction temperature, reaction time, and concentration of GOx are carried out to explore the optimal catalytic conditions (Fig. S5). With increasing volume of $TiSe_{2-x}$@Au, the concentration of PPD, pH, temperature, and reaction time, the absorption intensities at 413 nm increase quickly in a certain range and then become relatively stable so that the optimal parameters can be identified. The concentration of GOx is determined to be 1 mg/mL to ensure good catalytic effects. It should be noted that the $TiSe_{2-x}$ becomes amorphous after reaction (Fig. S6a) while the $TiSe_{2-x}$@Au nanocomposites show great stability as the crystal planes of $TiSe_{2-x}$@Au nanocomposites are intact before and after the reaction (Fig. S6b), indicating the decoration of AuNPs can also enhance the stability of $TiSe_{2-x}$. To highlight the reusability of the $TiSe_{2-x}$@Au nanocomposites, the $TiSe_{2-x}$@Au nanocomposites were collected after the reaction by centrifugation. The recycled $TiSe_{2-x}$@Au nanocomposites exhibit slight reduction in catalytic performance for the second cycle as the absorption intensity at 413 nm only reduces by 3.2% (Fig. S6c). The further reduction of catalytic performance for more cycles could be due to the aggregation or degradation of $TiSe_{2-x}$@Au nanocomposites.

The $TiSe_{2-x}$@Au colorimetric system is assessed with different concentrations of H_2O_2 or glucose under the optimized conditions (20 μL $TiSe_{2-x}$@Au nanocomposites, 50 mM PPD, pH 5.6, 40 °C, 40 min and 1 mg/mL GOx). In 5 mM H_2O_2, the color of PPD + H_2O_2 + $TiSe_{2-x}$@Au changes from colorless to brown-yellow and deepens gradually. The absorption intensity at 413 nm increases with addition of H_2O_2 (Fig. 5a). As shown in Fig. 5b and c, the catalytic system for H_2O_2 exhibits a good linear relationship in the range of 0.004 mM–1 mM. The corresponding equation is $y = 1.6534x + 0.0874$ ($R^2 = 99.85\%$) with a detection limit (LOD) of 0.0024 mM (LOD = 3s/κ, s = 0.001297, and κ = 1.6534, where s represents the standard deviation of 10 blank groups and κ represents the slope in the linear relationship). Additionally, Fig. 5b shows a slope difference at higher concentration of H_2O_2, indicating that another reaction occurs with further addition of H_2O_2. It may be due to the different reaction states of the nanomaterials with H_2O_2 because it is easier for H_2O_2 to react with $TiSe_{2-x}$@Au at low concentrations (Mi et al., 2018; Peng et al., 2019; Song et al., 2020).

Encouraged by the superior sensitivity of the $TiSe_{2-x}$@Au colorimetric system for H_2O_2, the detection of glucose follows the reaction (1):

$$\text{Glucose} + O_2 \rightarrow H_2O_2 + \text{Gluconic acid.} \quad (1)$$

As GOx catalyzes glucose to form H_2O_2 and gluconic acid, the generated H_2O_2 is proportional to the original concentration of glucose. Subsequently, with reference to the linear detection range of H_2O_2, the detection ability of glucose in the range of 0 mM–1 mM of the $TiSe_{2-x}$@Au catalytic system is studied. The color change and absorbance evolution with increasing concentrations of glucose are similar to those of H_2O_2 (Fig. 5d). Fig. 5e and f show that the linear range is 0.015 mM–0.6 mM with the equation $y = 0.9834x + 0.0916$ ($R^2 = 99.79\%$) with the LOD of 0.0037 mM (LOD = 3s/κ, s = 0.001198, and κ = 0.9834), which is superior to that of most other nanomaterials-based glucose colorimetric methods (Table S3). Also, the reaction time is comparable to other colorimetric methods.

3.4. Glucose detection in human serum

The common potential interferences in serum such as biomolecules (Suc, Gly, AA, GSH, CA, and urea) and metal ions (K^+, Na^+, Ca^{2+}, Mg^{2+},

Table 1
Comparison of the blood glucose detection results using the $TiSe_{2-x}$@Au catalytic system with those obtained clinically in the hospital using a glucose meter.

Serum sample	Detection result (mM)	Result from hospital (mM)	RSD (n = 3) (%)
Sample 1	4.24	4.32	1.78
Sample 2	10.05	10.05	1.74
Sample 3	4.21	4.04	3.65
Sample 4	4.70	4.78	1.36
Sample 5	11.02	10.41	1.43
Sample 6	6.71	6.36	5.92
Sample 7	4.20	4.21	4.19
Sample 8	8.05	7.36	3.37
Sample 9	7.29	7.97	4.23
Sample 10	8.82	8.94	2.10
Sample 11	6.96	7.68	2.10
Sample 12	4.89	5.01	2.26

and Zn^{2+}) are set as the control groups to demonstrate the specificity of the $TiSe_{2-x}$@Au catalytic system. Compared with the significant absorbance by glucose, the common interferences do not show noticeable absorbance at 413 nm even though the concentration (6 mM) is 10 times that of glucose (0.6 mM) (Fig. S7). The difference in the absorbance at 413 nm between glucose and the common interferences is significant ($p < 0.05$), revealing that the $TiSe_{2-x}$@Au catalytic system has a specific glucose detection capability.

This colorimetric method is further applied to the detection of blood glucose in human serum samples. A linear relationship between the absorption intensity at 413 nm and blood glucose is established for the $TiSe_{2-x}$@Au system by analyzing 7 serum samples with known glucose concentrations determined by a commercial blood glucose meter from the hospital. As shown in Fig. S8a, the absorption at 413 nm increases gradually with blood glucose concentration, and the linear range from 0.12 mM to 0.52 mM can be fitted by the equation $y = 0.4881x + 0.0812$ ($R^2 = 99.43\%$) (Fig. S8b). Afterward, 12 serum samples with unknown glucose concentrations are measured based on the calibration chart. Fig. S8c shows that the 12 serum samples all produce obvious absorption peaks at 413 nm and the intensities are converted into glucose concentrations (Table 1). Compared with those measured in the hospital, the results obtained by the $TiSe_{2-x}$@Au system are highly consistent with a relative standard deviation (RSD) of less than 6%), suggesting that this colorimetric method has great accuracy and prospect in clinical blood glucose monitoring.

4. Conclusion

A simple and sensitive colorimetric method is designed and demonstrated for glucose detection using Se-vacancy-rich $TiSe_{2-x}$@Au nanocomposites as nanozymes. The $TiSe_{2-x}$@Au nanocomposites are synthesized by an easy reduction technique. Compared with $TiSe_{2-x}$ nanosheets, the Se-vacancy-rich $TiSe_{2-x}$@Au nanocomposites exhibit enhanced peroxidase-like activity to selectively catalyze PPD to oxPPD which shows an absorption peak at 413 nm in the presence of H_2O_2, and visible changes from colorless to brown. This selective reaction avoids the interference by possible self-oxidation of PPD. Theoretical calculations reveal that the Se vacancies inhibit the free reaction and promote both the activity and selectivity of PPD oxidation. By coupling with GOx, the $TiSe_{2-x}$@Au colorimetric system exhibits a wide linear range of 0.015 mM–0.6 mM and a low LOD of 0.0037 mM in glucose detection. The clinical feasibility is confirmed with human serum samples and the performance is comparable to that of a commercial glucose meter. The colorimetric system has great potential in clinical application and the results provide insights into the future design of nanozymes.

CRediT authorship contribution statement

Caixia Sun: Investigation, Methodology, Writing – original draft. **Xue Zhang:** Investigation, Methodology. **Hao Huang:** Conceptualization, Supervision, Writing – original draft, Writing – review & editing. **Ya Liu:** Investigation. **Xianwei Mo:** Investigation. **Yufei Feng:** Writing – review & editing. **Jiahong Wang:** Formal analysis, Writing – original draft. **Wenhua Zhou:** Writing – review & editing. **Paul K. Chu:** Writing – review & editing. **Xue-Feng Yu:** Writing – review & editing. **Wenxin Liu:** Conceptualization, Writing – review & editing, Supervision, Project administration.

Declaration of competing interest

The authors declare that they have no known competing financial interests or personal relationships that could have appeared to influence the work reported in this paper.

Data availability

Data will be made available on request.

Acknowledgments

This work was supported by the National Natural Science Foundation of China (22102208, X.Z.; 31971368, W.Z.), Guangdong Basci and Applied Basic Research Foundation (2020A1515010639, W.L.; 2022A1515011959, H.H.; 2023A1515030178, X.Z.; 2020B1515120040, W.Z.; 2021A1515220027, Y.F.; 2022B1515020029, W.Z.), Science and technology special competitive allocation project of Zhanjiang City (2021A05147, W.L.; 2021A05130, X.M.), PhD Start-up Program of Central People's Hospital of Zhanjiang (2020A07, W.L.), Young Elite Scientist Sponsorship Program by CAST (No. YESS20210226, J.W.), Youth Innovation Promotion Association Chinese Academy of Sciences (2020354, J.W.), Talent introduction special funds of Lingnan Normal University (ZL2021013, Y.F.), City University of Hong Kong Strategic Research Grant (SRG 7005505, P.K.C.), and City University of Hong Kong Donation Research Grant (DON-RMG 9229021, P.K.C.).

Appendix A. Supplementary data

Supplementary data to this article can be found online at https://doi.org/10.1016/j.bios.2023.115665.

References

BlÖchl, P.E., 1994. Phys. Rev. B 50, 17953–17979.
Cai, X., Luo, Y., Liu, B., Cheng, H.M., 2018. Chem. Soc. Rev. 47, 6224–6266.
Chang, Y., Zhai, P., Hou, J., Zhao, J., Gao, J., 2021. Adv. Energy Mater. 12, 2102359.
Chen, T.M., Wu, X.J., Wang, J.X., Yang, G.W., 2017. Nanoscale 9, 11806–11813.
Cheng, X., Sun, L., Li, R., Huang, Y., Xu, H., Wang, Z., Li, Z.L., Jiang, H., Ma, J., 2019. Mikrochim. Acta 186, 731.
Choi, W., Choudhary, N., Han, G.H., Park, J., Akinwande, D., Lee, Y.H., 2017. Mater. Today 20, 116–130.
Durgaryan, A.A., Arakelyan, R.A., Durgaryan, N.A., 2013. Russ. J. Gen. Chem. 84, 1095–1100.
Gao, L., Zhuang, J., Nie, L., Zhang, J., Zhang, Y., Gu, N., Wang, T., Feng, J., Yang, D., Perrett, S., Yan, X., 2007. Nat. Nanotechnol. 2, 577–583.
Gong, I.Y., Cheung, M.C., Read, S., Na, Y., Lega, I.C., Lipscombe, L.L., 2021. Diabetologia 64, 540–551.
Han, J.H., Kim, H.K., Baek, B., Han, J., Ahn, H.S., Baik, M.H., Cheon, J., 2018. J. Am. Chem. Soc. 140, 13663–13671.
Hong, C., Chen, L., Wu, C., Yang, D., Dai, J.-Y., Huang, Z., Cai, R., Tan, W., 2021. Nano Res. 15, 1587–1592.
Hong, J., Jin, C., Yuan, J., Zhang, Z., 2017. Adv. Mater. 29, 1606434.
Hussein, S., Mohamed, D., Hafez, R., 2019. The Egyptian. JAMA Intern. Med. 31, 171–177.
Jiang, G., Lin, T., Qin, Y., Zhang, X., Hou, L., Sun, Y., Huang, J., Liu, S., Zhao, S., 2020. Chem. Commun. 56, 10847–10850.
Jiao, L., Yan, H., Wu, Y., Gu, W., Zhu, C., Du, D., Lin, Y., 2020. Angew. Chem., Int. Ed. Engl. 59, 2565–2576.
Khan, R., Radoi, A., Rashid, S., Hayat, A., Vasilescu, A., Andreescu, S., 2021. Sensors 21, 3369.

Kim, M., Lee, S.H., Park, K.S., Kim, E.J., Yeo, S., Ha, I.H., 2021. BMC Endocr. Disord. 21, 209.
Kyriakou, T.C., Papageorgis, P., Christodoulou, M.I., 2021. Int. J. Mol. Sci. 22, 9322.
Li, D., Li, N., Zhao, L., Xu, S., Sun, Y., Ma, P., Song, D., Wang, X., 2020. ACS Appl. Nano Mater. 3, 11600–11607.
Li, L.J., O'Farrell, E.C., Loh, K.P., Eda, G., Ozyilmaz, B., Castro Neto, A.H., 2016. Nature 529, 185–189.
Li, N., Green, J.R., Wang, J., 2007. Chem. Phys. Lett. 447, 241–246.
Liang, X., Han, L., 2020. Adv. Funct. Mater. 30, 2001933.
Ling, Y., Wu, Y., Wang, C., Liu, C., Lu, S., Zhang, B., 2021. ACS Catal. 11, 9471–9478.
Liu, C., Im, S.H., Yu, T., 2021. Catalysts 11, 343.
Liu, H., Chen, Q., Cheng, X., Wang, Y., Zhang, Y., Fan, G., 2020. Sensor. Actuat. B-Chem. 314, 128067.
Liu, M., Zhao, H.M., Chen, S., Yu, H.T., Quan, X., 2012. ACS Nano 6, 3142–3151.
Lu, L., Zhu, Y., Shi, C., Pei, Y.T., 2016. Carbon 109, 373–383.
Mi, Y., Lei, X., Han, H., Liang, J., Liu, L., 2018. Anal. Methods 10, 4170–4177.
Miao, L., Jiao, L., Tang, Q., Li, H., Zhang, L., Wei, Q., 2019. Sensor. Actuat. B-Chem. 288, 60–64.
Peng, C., Xing, H., Fan, X., Xue, Y., Li, J., Wang, E., 2019. Anal. Chem. 91, 5762–5767.
Perdew, J.P., Burke, K., Ernzerhof, M., 1996. Phys. Rev. Lett. 77, 3865.
Pullano, S.A., Greco, M., Bianco, M.G., Foti, D., Brunetti, A., Fiorillo, A.S., 2022. Theranostics 12, 493–511.
Ritter, J.J., Schmitz, G.H., 1929. J. Am. Chem. Soc. 51 (5), 1587–1589.
Rohaizad, N., Mayorga-Martinez, C.C., Fojtu, M., Latiff, N.M., Pumera, M., 2021. Chem. Soc. Rev. 50, 619–657.
Sengupta, P., Pramanik, K., Datta, P., Sarkar, P., 2020. Biosens. Bioelectron. 154, 112072.
Shamsipur, M., Safavi, A., Mohammadpour, Z., 2014. Sensor. Actuat. B-Chem. 199, 463–469.
Shen, P., Li, X., Luo, Y., Guo, Y., Zhao, X., Chu, K., 2022. ACS Nano 16, 7915–7925.
Singh, G., Ghosh, A., Pandey, P., Kushwaha, A., Kumar Gaur, U., Sharma, M., 2022. Mater. Lett. 317, 132084.
Song, C., Ding, W., Zhao, W., Liu, H., Wang, J., Yao, Y., Yao, C., 2020. Biosens. Bioelectron. 151, 111983.
Song, Y., Qu, K., Zhao, C., Ren, J., Qu, X., 2010. Adv. Mater. 22, 2206–2210.
Sun, J., Zhao, J., Wang, L., Li, H., Yang, F., Yang, X., 2018. ACS Sens. 3, 183–190.
Sun, Y., Darling, A.J., Li, Y., Fujisawa, K., Holder, C.F., Liu, H., Janik, M.J., Terrones, M., Schaak, R.E., 2019. Chem. Sci. 10, 10310–10317.
Urban, P.L., Goodall, D.M., Bergstrom, E.T., Bruce, N.C., 2006. Anal. Biochem. 359, 35–39.
Via, V.D., Halter, J.P., Gerull, S., Arranto, C., Tichelli, A., Heim, D., Passweg, J.R., Medinger, M., Cesana-Nigro, N., 2020. In Vivo 34, 3545–3549.
Wu, J., Wang, X., Wang, Q., Lou, Z., Li, S., Zhu, Y., Qin, L., Wei, H., 2019. Chem. Soc. Rev. 48, 1004–1076.
Wu, X., Chen, T., Chen, Y., Yang, G., 2020. J. Mater. Chem. B 8, 2650–2659.
Xu, Y., Wang, X., Ding, C., Luo, X., 2021. ACS Appl. Mater. Interfaces 13, 20388–20396.
Xue, M., Mao, W., Chen, J., Zheng, F., Chen, W., Shen, W., Tang, S., 2021. Analyst 146, 6726–6740.
Yao, F., Cai, Y., Xiao, Z., Zhang, G., Xie, R.-J., Jin, C., 2020. 2D Mater. 8, 025004.
Yu, J., Ma, D., Mei, L., Gao, Q., Yin, W., Zhang, X., Yan, L., Gu, Z., Ma, X., Zhao, Y., 2018. J. Mater. Chem. B 6, 487–498.
Zhang, D., Zhao, G., Li, P., Zhang, Y., Qiu, W., Shu, J., Jiang, Y., Dou, S.X., Sun, W., 2018. Chemistry 24, 1193–1197.
Zhang, W., You, J.B., Liu, J., Xiong, X., Li, Z., Png, C.E., Wu, L., Qiu, C.W., Zhou, Z.K., 2021. Nano Lett. 21, 8979–8986.
Zhang, X., Li, G., Wu, D., Li, X., Hu, N., Chen, J., Chen, G., Wu, Y., 2019. Biosens. Bioelectron. 137, 178–198.
Zhang, Y., Schmid, Y.R.F., Luginbuhl, S., Wang, Q., Dittrich, P.S., Walde, P., 2017. Anal. Chem. 89, 5484–5493.

Supporting Information

Selective oxidation of p-phenylenediamine for blood glucose detection enabled by Se-vacancy-rich $TiSe_{2-x}$@Au nanozyme

Caixia Sun,[a, b, e] Xue Zhang,[b] Hao Huang,[b*] Ya Liu,[a] Xianwei Mo,[a] Yufei Feng,[c] Jiahong Wang,[b] Wenhua Zhou,[b, d] Paul K. Chu,[f] Xue-Feng Yu,[b, d] Wenxin Liu[a*]

[a] Zhanjiang Institute of Clinical Medicine, Zhanjiang Central Hospital, Guangdong Medical University, Zhanjiang, 524045, People's Republic of China

[b] Shenzhen Key Laboratory of Micro/Nano Biosensing, Shenzhen Institute of Advanced Technology, Chinese Academy of Sciences, Shenzhen, 518055, People's Republic of China

[c] Life Science and Technology School, Lingnan Normal University, Zhanjiang 524048, People's Republic of China

[d] Biomedical Imaging Science and System Key Laboratory, Chinese Academy of Sciences, Shenzhen, 518055, People's Republic of China

[e] The First Clinical Medical School, Guangdong Medical University, Zhanjiang, 524023, People's Republic of China

[f] Department of Physics, Department of Materials Science and Engineering, and Department of Biomedical Engineering, City University of Hong Kong, Tat Chee Avenue, Kowloon, Hong Kong, China

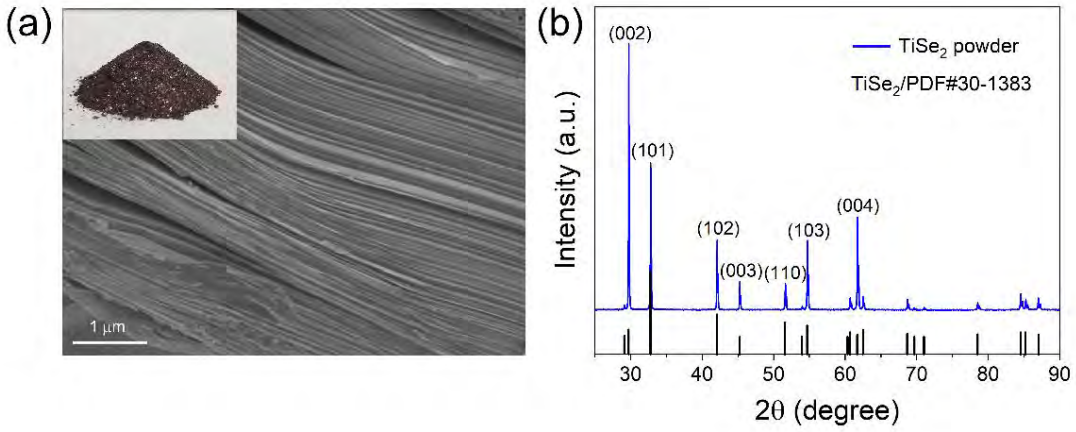

Fig. S1. (a) SEM image of $TiSe_2$ powders (inset showing a photo of the $TiSe_2$ powders) and (b) XRD pattern of $TiSe_2$ powders.

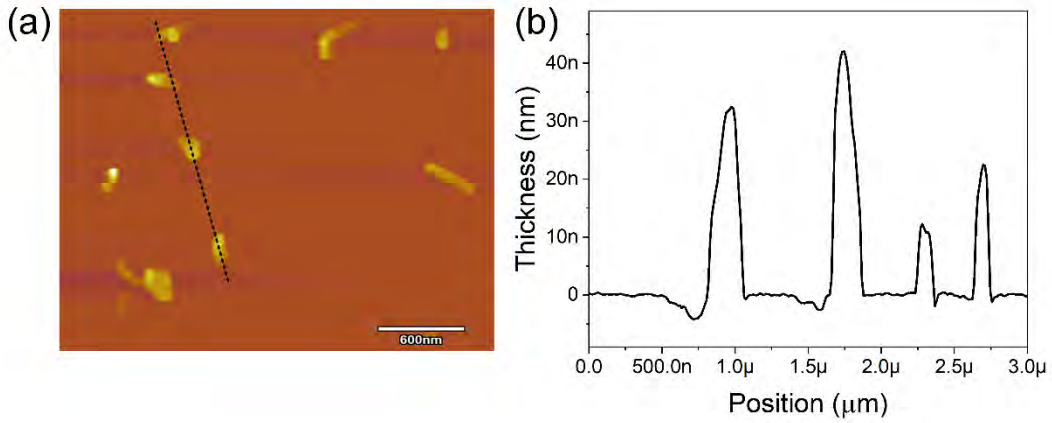

Fig. S2. (a) AFM image of $TiSe_{2-x}$ nanosheets and (b) Thickness line scan of $TiSe_{2-x}$ nanosheets.

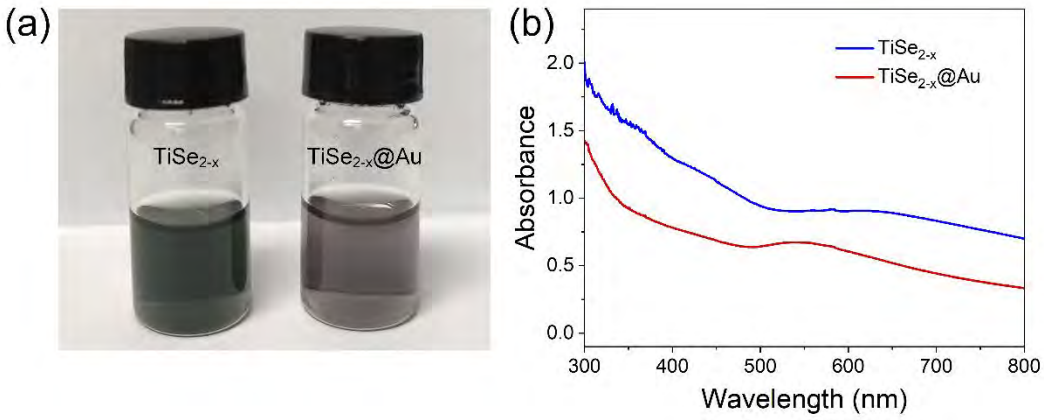

Fig. S3. (a) Photo of $TiSe_{2-x}$ nanosheets and $TiSe_{2-x}$@Au nanocomposites dispersed in DMF and (b) UV-vis spectra of $TiSe_{2-x}$ nanosheets (blue line) and $TiSe_{2-x}$@Au nanocomposites (red line).

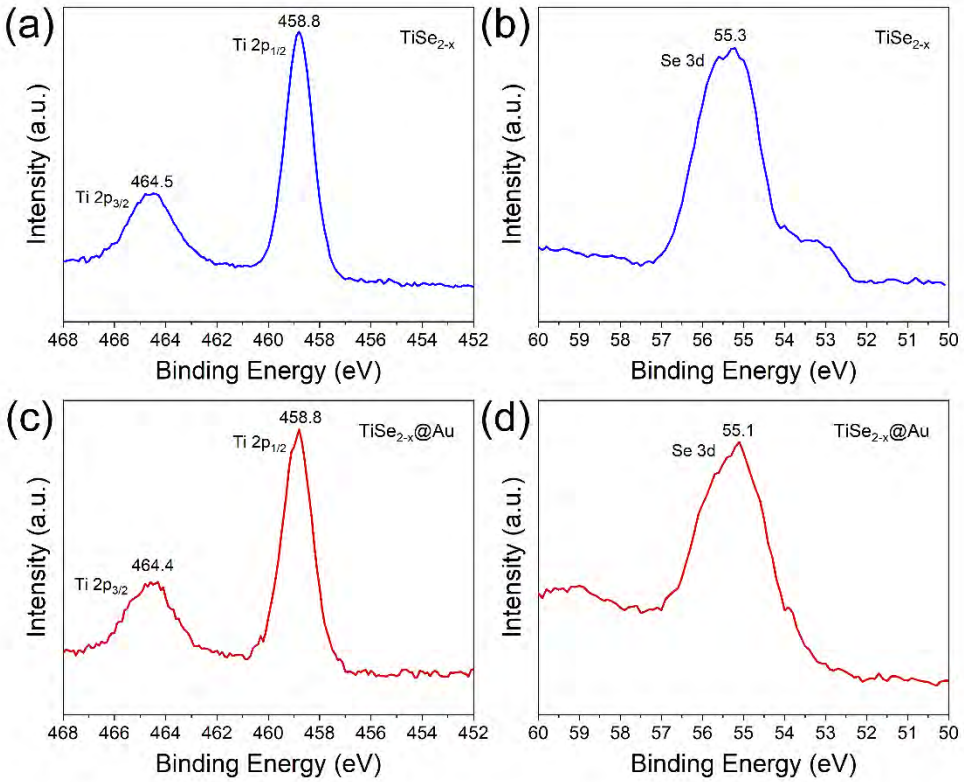

Fig. S4. XPS Ti 2*p* and Se 3*d* spectra of $TiSe_{2-x}$ nanosheets and $TiSe_{2-x}$@Au nanocomposites.

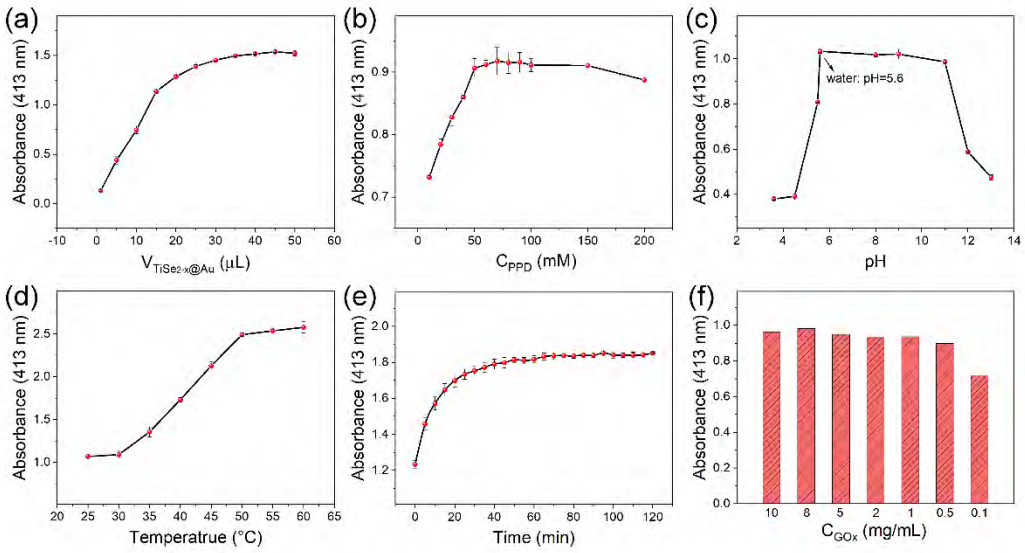

Fig. S5. Optimized experiments of the $TiSe_{2-x}$@Au colorimetric system: (a) Concentration of $TiSe_{2-x}$@Au nanocomposites (n=3), (b) Concentration of PPD (n=3), (c) pH (n=3), (d) Reaction temperature (n=3), (e) Reaction time (n=3), and (f) Concentration of GOx.

The optimal concentration of $TiSe_{2-x}$@Au in the reaction is determined by adjusting the volume of $TiSe_{2-x}$@Au with a fixed concentration. As shown in Fig. S5a, the absorbance at 413 nm increases linearly until the volume of $TiSe_{2-x}$@Au is 20 μL. Therefore, a volume of 20 μL is chosen as the optimal value. Similarly, when the concentration of PPD increases to 50 mM, the absorbance rises to a stable plateau (Fig. S5b) and 50 mM PPD is the optimum value for the colorimetric reaction. The pH range is adjusted by distilled water or HAc-NaAc buffer and NaOH solution. As

shown in Fig. S5c, the absorbance at 413 nm is the largest in an acidic solution (pH = 5.6 measured by an acidity meter). Therefore, 5.6 is the optimum pH. Similar phenomenon has been reported in previous work (Jiang et al., 2020), and this could be due to the adsorbed state and the stability difference of the PPD under different pH. The absorbance at 413 nm increases gradually from 25 °C to 60 °C (Fig. S5d) and the optimal temperature is determined to be 40 °C because GOx can better catalyze the oxidation of glucose between 30 °C and 40 °C to promote the subsequent experiments. In the presence of 0.5 mM H_2O_2, the reaction time of the PPD + H_2O_2 + $TiSe_{2-x}$@Au system is varied continuously under the aforementioned optimized conditions and the absorbance becomes after 40 min (Fig. S5e). Hence, 40 min is the optimal reaction time of the colorimetric system. Finally, the concentration of GOx is investigated in the range between 0.1 mg/mL and 10 mg/mL. With the exception of 0.1 mg/mL GOx, there is no significant difference in the absorbance for the other concentrations of GOx (Fig. S5f). To ensure good catalytic effects, the amount of enzyme should be reduced as much as possible and the concentration of GOx is determined to be 1 mg/mL.

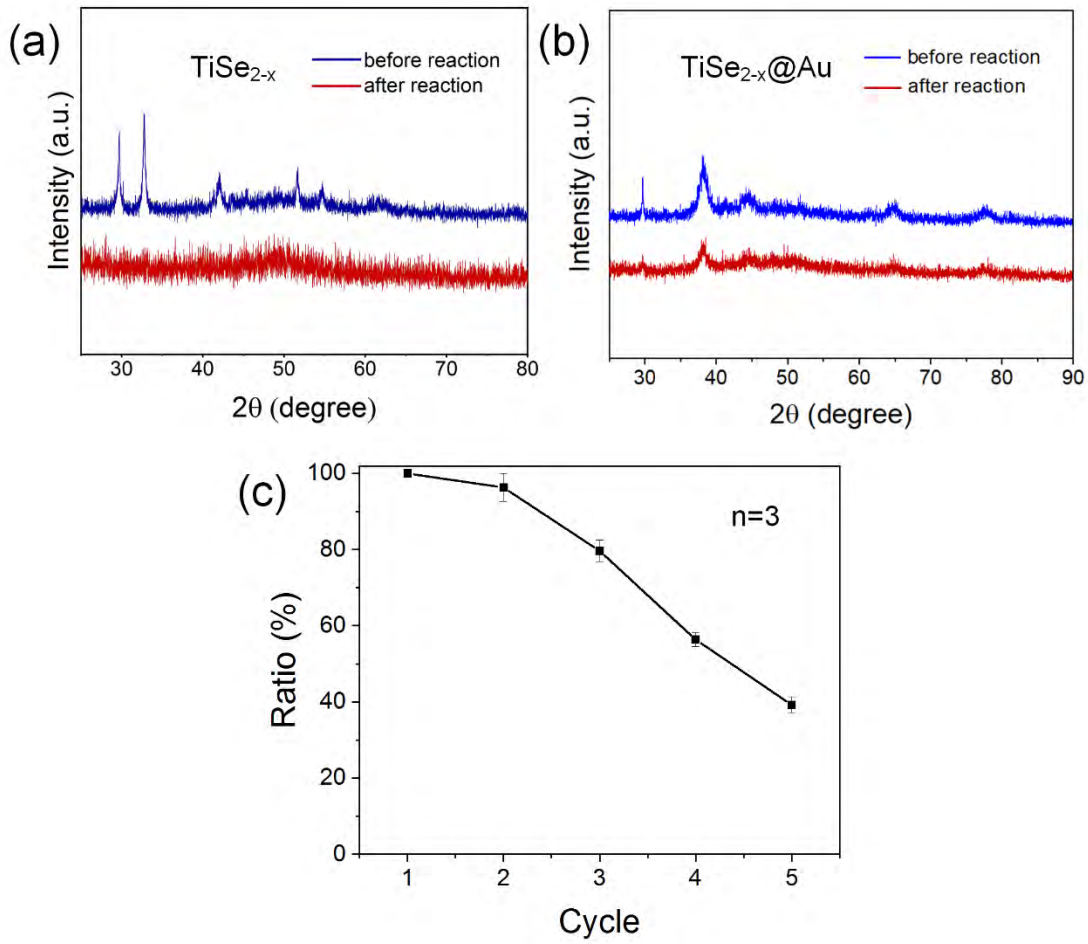

Fig. S6. (a, b) XRD patterns of $TiSe_{2-x}$ and $TiSe_{2-x}$@Au before (blue line) and after (red line) the reaction. (c) Recycling of the $TiSe_{2-x}$@Au for the selective reaction. The intensity ratio at 413 nm for 5 cycles.

Table S1. DFT-optimized adsorption energies of PPD adsorbing on $TiSe_2$ for two adsorption geometries: parallel and vertical.

Adsorption sites	Adsorption Energies (eV)
Parallel	-0.63
Vertical	-2.82

Table S2. DFT-optimized adsorption energies of PPD adsorbing on $TiSe_{2-x}$ for seven adsorption geometries: parallel 1-2, parallel 2-7, parallel 6-34, vertical 1-2, vertical 6-2, vertical 6-3, and vertical 2-7.

Adsorption sites	Adsorption Energies (eV)
Parallel 1-2	0.71
Parallel 2-7	0.56
Parallel 6-34	0.80
Vertical 1-2	-2.73
Vertical 6-2	-2.86
Vertical 6-3	-3.00
Vertical 2-7	-2.84

Table S3. Comparison of nanomaterials-based colorimetric methods for glucose detection.

Nanomaterials	Substrates	Absorbance peak (nm)	Reaction time (min)	Linear range (mM)	LOD (mM)	Refs.
Ti_3C_2 NSs	TMB	652	-	0.01 - 0.32	0.00882	(Wu et al., 2020)
Cu-Ag-RGO	TMB	652	30	0.001 - 0.03	0.00382	(Darabdhara et al., 2017)
WSe_2 NSs	TMB	652	-	0.01 - 0.06	0.01	(Chen et al., 2017)
Au@WSe_2	TMB	652	30	0.01 - 0.5	0.00366	(Hong et al., 2021)
$MoSe_2$ NSs	TMB	652	-	0.04 - 0.4	0.028	(Jiang et al., 2020)
Ce-$MoSe_2$ NSs	TMB	652	35	0.01 - 0.05	0.00169	(Singh et al., 2022)
Cys-MoS_2 NFs	ABTS	414	30	0.05 - 1	0.03351	(Yu et al., 2018)
CoOOH@Cu NSs	OPD	450	20	0.025 - 2.5	0.00738	(Cheng et al., 2022)
OSiNDs	PPD	510	20	0.0005 - 0.5	0.00036	(Li et al., 2020)
$TiSe_{2-x}$@Au	PPD	413	40	0.015 - 0.6	0.0037	This work

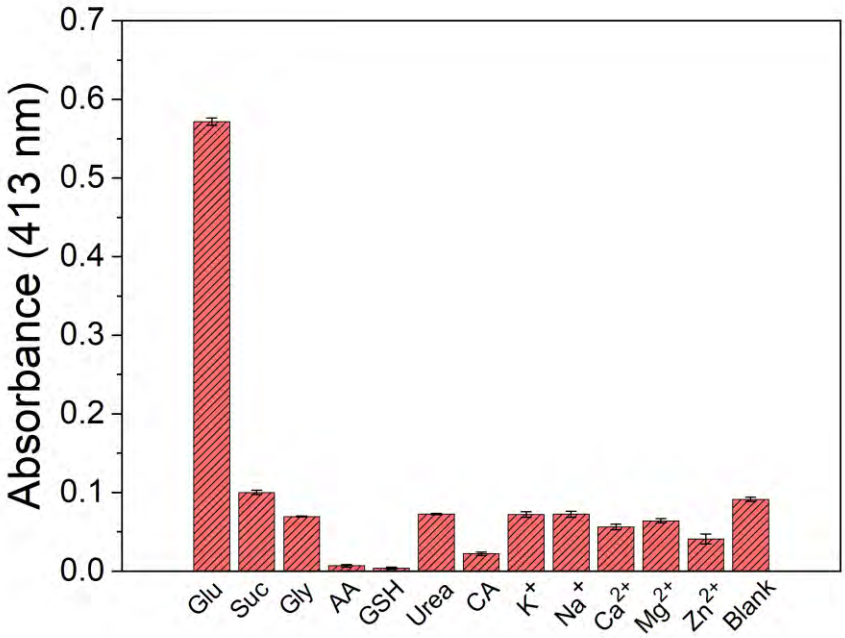

Fig. S7. Specificity of the $TiSe_{2-x}$@Au catalytic system for glucose detection (Glucose concentration = 0.6 mM; interference concentration = 6 mM) (n=3).

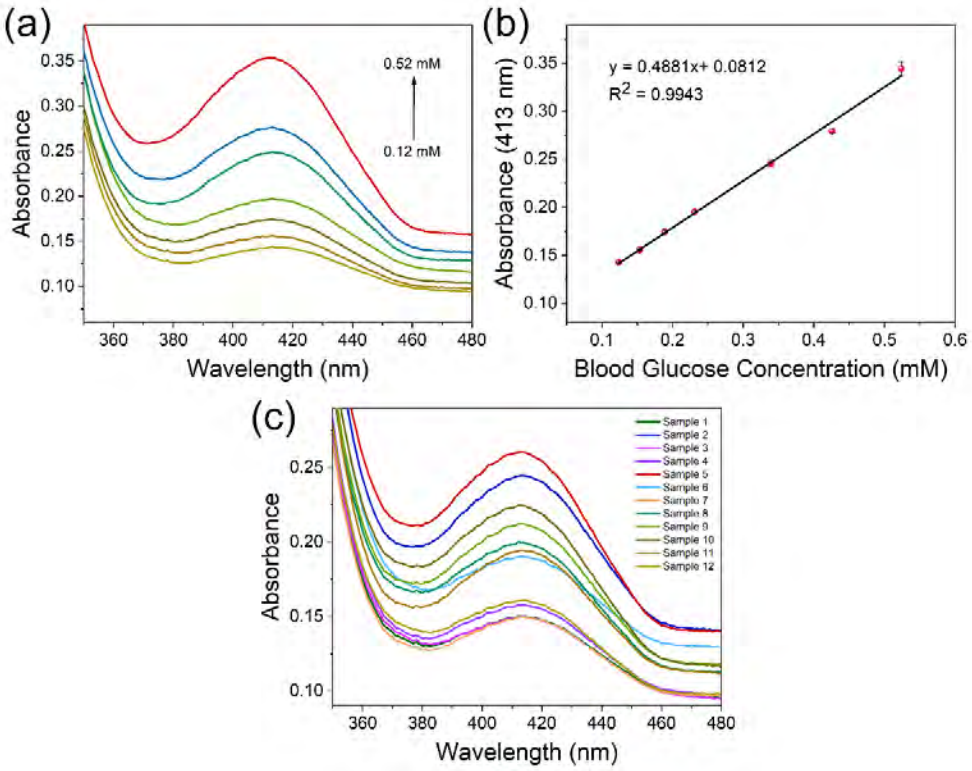

Fig. S8 (a) UV–vis spectra versus blood glucose concentrations in the serum samples for the $TiSe_{2-x}$@Au colorimetric system, (b) Linear plot of absorption intensity at 413 nm versus blood glucose concentration (n=3), and (c) Changes of peak intensity at 413 nm for different blood glucose concentrations in the serum samples.

References

Chen, T.M., Wu, X.J., Wang, J.X., Yang, G.W., 2017. Nanoscale 9, 11806-11813.

Cheng, H., Wang, Z., Sun, H., Chen, B., Huang, J., Jia, R., He, X., Wang, K., 2022. Chem. Commun. 58, 13487-13490.

Darabdhara, G., Sharma, B., Das, M.R., Boukherroub, R., Szunerits, S., 2017. Sensor Actuat. B-Chem. 238, 842-851.

Hong, C., Chen, L., Wu, C., Yang, D., Dai, J.-Y., Huang, Z., Cai, R., Tan, W., 2021. Nano Res. 151, 111983.

Jiang, G., Lin, T., Qin, Y., Zhang, X., Hou, L., Sun, Y., Huang, J., Liu, S., Zhao, S., 2020. Chem. Commun. 56, 10847-10850.

Li, D., Li, N., Zhao, L., Xu, S., Sun, Y., Ma, P., Song, D., Wang, X., 2020. ACS Appl. Nano Mater. 3, 11600-11607.

Singh, G., Ghosh, A., Pandey, P., Kushwaha, A., Kumar Gaur, U., Sharma, M., 2022. Mater. Lett. 317, 132084.

Wu, X., Chen, T., Chen, Y., Yang, G., 2020. J. Mater. Chem. B 8, 2650-2659.

Yu, J., Ma, D., Mei, L., Gao, Q., Yin, W., Zhang, X., Yan, L., Gu, Z., Ma, X., Zhao, Y., 2018. J. Mater. Chem. B 6, 487-498.